Modeling and optimizing chromate photo-precipitation with iodide exciting under UV irradiation

Tayebeh Rasolevandi[a], Hossein Azarpira[b], Amir Hossein Mahvi[a,c,]*

[a]*Environmental Health Engineering, School of Public Health, Tehran University of Medical Sciences, Tehran, Iran,
emails: ahmahvi@yahoo.com/ahmahvi95@gmail.com (A.H. Mahvi)*
[b]*Department of Environmental Health Engineering, Social Determinants of Health Research Center,
Saveh University of Medical Sciences, Saveh, Iran*
[c]*Center for Solid Waste Research (CSWR), Institute for Environmental Research (IER), Tehran University of Medical Sciences,
Tehran, Iran*

ABSTRACT

This study aims to develop a process based on the UV irradiation of iodide (UI) to create reducer agents for photo-precipitation of the chromate. To perform the RSM-based optimization, the R 3.0.3 software was employed. A central composite design function was implanted that could fit and model a standard response surface into the coded experimental data. According to the highest R^2 value (multiple R^2: 0.9986 and adjusted R^2: 0.9974), the lowest P-value (2.2×10^{-16}), the lowest AIC (12.27), and the most insignificant lack-of-fit (0.6711) corresponding to the second-order model were chosen for optimization. Based on this model, the stationary for iodide dose (mg L^{-1}), pH, time (min), and initial Cr concentration were 0.3 mg L^{-1}, 7, 50 min, and 0.5 mg L^{-1}, respectively, and photo-precipitation performance reached to 94.42%. Base on this pseudo-first-order kinetic model, the observed rate constant (k_{obs}) and the related rate (r_{obs}), respectively altered from 5.67 to 15.21 min^{-1} and from 0.3317 to 2.372 mg L^{-1} min^{-1} by the increase of Cr concentration from 5 to 20 mg L^{-1}. Also, with increasing of Cr concentration from 5 to 20 mg L^{-1}, E_{EO} increased from 5.67 to 15.21 (kinetic model) and from 5.11 to 18.45 (figure-of-merit model) kW h m^{-3}.

Keywords: Photo-precipitation; Iodide anion; Hydrated electron; Kinetics; Energy consumption.

1. Introduction

Chrome is one of the most serious environmental contaminants, with various oxidation of 6 to –2 [1–3]. In an aquatic system, hexavalent chromium (Cr (VI)), such as chromate [$CrO_4^{2\bullet-}$, $HCrO_4^-$], is highly mobile and soluble reactive that can influence large-volume aquifers, and affect biological systems due to its strong oxidizing properties [4,5]. Hexavalent chromium, Cr(VI), is a common contaminant in soil and groundwater and is classified as a significant pollutant by the US Environmental Protection Agency (EPA) [6,7]. It is more toxic (about 500–1,000 times) than Cr(III) [8,9]. The EPA has recommended a maximum contaminant level of 0.1 and 0.05 mg L^{-1} for Cr(VI) for inland surface and potable waters, respectively. A few processes have been applied for the removal of heavy metals from industrial wastewaters [10–13]. Several typical methods are usually applied to eliminate or lessen the concentration of Cr(VI) and heavy metals, including adsorption onto solid adsorbents [14–16], magnetic nanocarbon [17], reduction [18,19], electrochemical processes [20], membrane filtration [21], precipitation [22], ion exchange. Scientists are studying new and alternative technologies to develop efficient and cost-effective treatments for the removal of such pollutants. To overcome these problems, the application of UV-based reduction presents several advantages including being

* Corresponding author.

done in one-step, being done *in situ*, being pH-independent, involving fast mass transfer and complete ions elimination and molecules [23]. Typically, the generation of the reductive agents requires the addition of some inorganic anions such as sulfite, carboxyl, or iodide that are commonly found in the well waters [23,24]. Compared with other anions, iodide has two important advantage (1) much more efficiently of UV light adsorption (ε_{I^-}, 254 = 220 M^{-1} cm^{-1} according to Eq. (1) and high quantum yields of e_{aq}^- (e.g., 0.286 mol E^{-1} at 253.7 nm) [25,26].

$$I^- + h\nu_{254} \rightarrow I^-_{CTTS} \rightarrow I + e_{aq}^- \tag{1}$$

RSM can optimize the conditions of various experimental processes by using a limited set of data. To perform an RSM-based optimization, the following steps were followed. First, the experimental data were coded and the coded values were implemented to create an experimental design. Then, a model of the associated response surface was fitted into the coded data to obtain the modeled response. Finally, the conditions were optimized [27]. Therefore, the present study was undertaken: (1) performance and efficiency of hexavalent chromium precipitation by the I$^-$/UV process, (2) effects of the typical factors on I$^-$ radical/UV process and optimization them with RSM, (3) energy consumption estimates and kinetics of hexavalent chromium precipitation by I$^-$/UV process, (4) effect of co-present species in water matrix on I$^-$/UV process, (5) mechanisms involved in the precipitation of hexavalent chromium preliminarily by I$^-$/UV process, (6) produced sludge in I$^-$/UV process.

2. Martial and methods

2.1. Materials and reactor set up

Ultra-pure sodium iodide was obtained from Alfa Aesa Co., (Massachusetts, USA, 99.5% purity). Other analytic-grade chemical reagents were obtained from Sinopharm Chemical Reagent Co., Ltd., (Shanghai, China, 99.5% purity). Deionized water was used throughout the work. The photocatalytic experiments were performed in a sealed reactor made of tubular glass with 150 mL capacity. To irradiate UV light on the examined samples, the photoreactor was covered with a quartz sleeve that was placed in the central part of the reactor and contained a low-pressure mercury lamp (UVC; 90%) with 87 µW cm^{-2} radiation flux and 11 W power. The distance between the lamp and the surface of the quartz sleeve was adjusted to 1 cm and the lamp radiated 254 nm rays. The intensity of the irradiated UV light was measured by a UVC 512 light meter. Fig. 1 presents the schematic view of the photo-reactor setup.

2.2. Analytical methods

To optimize the photocatalytic process, the effect of pH (3–10), initial Cr concentration (100–300 mg L^{-1}) and reaction time (5–20 min) on the photo-reduction of Cr were evaluated. To determine the extent of Cr reduction, the unreacted Cr molecules were separated by an atomic adsorption instrument. After measuring Cr concentration of the treated samples based on standard methods, the extent of Cr reduction was calculated through Eq. (2), in which Cr_0 and Cr_t are,

respectively, the concentration of Cr (mg L^{-1}) at the start and time t of the reaction.

$$Cr\ reduction = \frac{Cr_0 - Cr_t}{Cr_0} \tag{2}$$

Further, the reaction participants, that is, the reducing agents, were identified and approved by adding 50 mg L^{-1} of several electron acceptors to the reactor. The carbon tetrachloride, carbon disulfide electron acceptors were meant to act as reductive agent scavengers [28,29]. In addition, the effect of the Cl$^-$, NO$_3^-$, HCO^{3-}, and SO$_4^{2-}$ anions on photo-reduction of Cr was evaluated by ion chromatography.

2.3. Experimental design and optimization of the parameters

RSM optimizes the operating conditions with respect to a limited set of experimental data. In a typical RSM procedure, the experimental data are coded, the coded data are used to generate a design, a model of response surface is fitted into the data, the modeled response is displayed, and finally, the conditions are optimized [30]. The R 3.0.3 software was employed to perform RSM-based optimization. In the software, a central composite design (CCD) function is implemented that can fit and model a standard response surface into the coded experimental data. In this study, iodide dose (X_1), pH (X_2), the time (X_3), and initial concentration of Cr (X_4) were considered as the k independent variables in the CCD function [31,32]. These four variables are given in Table 1.

In total, 28 CCD runs including 16 (k^2) factorial points and 8 ($2k$) center points and 4 (k) axial points were designed. Then, the experimental methods were used to determine the output-dependent response, that is, the reduction efficiency (Υ), for each CCD run. In general, the R software takes advantage of three RSM models including the first-order response-surface (FO) model, the model of two-way interactions (TWI), and the full second-order (FSO) model. To determine the most proper response surface model, the experimental data were fitted into the three FO, TWI, and FSO models, and the best model was chosen for further analysis to achieve a reduced model and optimization of the reduction process [33]. The quality of the fitted models was assessed by the *P*-value, *F*-value, lack-of-fit, and multiple *R*-squared (R^2) statistical measures. According to these statistical measures, the model that had a smaller *p*-value, lower AIC, a greater *F*-value, insignificant lack-of-fit (or more lack-of-fit), and a higher R^2 was selected. The Akaike information criterion (AIC) is a relative quality estimation of statistical models for the given data set. Given the set of models for data, AIC estimates the quality of each model relative to each other. Therefore, AIC provides a tool for selecting a model. Furthermore, sufficient reliability of the fitted models was confirmed by ANOVA analysis [30,33]. Eq. (7) was adopted to correlate the independent variables to the experimental value of reduction efficiency (Υ):

$$\Upsilon = b_0 + \sum_{i=1}^{k} b_i X_i + \sum_{i=1}^{k} b_{ii} X_i^2 + \sum_{i=1}^{k-1} \sum_{j=1}^{k} b_{ij} X_i X_j + C \tag{3}$$

Here, b_0 is a constant value, b_i, b_{ii}, and b_{ij} are the regression coefficients for the linear, second-order, and interactive

Table 1
Actual and coded values of the independent variables used for experimental design

Variable	Symbol	Coded level				
		$-\alpha$	-1	0	$+1$	$+\alpha$
		Real values				
Iodide dose (mg L^{-1})	X_1	0.1	0.2	0.3	0.4	0.5
pH	X_2	4	5.5	7	8.5	10
Time (min)	X_3	10	30	50	70	90
Cr concentration (mg L^{-1})	X_4	0.5	1.5	2.5	3.5	4.5

effects, respectively, X_i and X_j refer to the input variables that influence the response, and c is the random error. Finally, the effective parameters were implemented in the solver utility of Excel to optimize the reduction conditions in the framework of the model equation suggested by RSM [32].

2.4. Kinetics and energy consumption

As it is almost impossible to quantify the photo-generated oxidative and reductive agents, the pseudo-first-order (PFO) kinetics model was adopted to study the kinetics of Cr-reduction. Based on this model, the observed reaction rate constant (k_{obs}) and rate (r_{obs}) were extracted from Eqs. (4) and (5), respectively.

$$\ln \frac{C_t}{C_0} = -k_{obs}t \tag{4}$$

$$r_{obs} = -k_{obs}C_{Cr} \tag{5}$$

Energy consumed for Cr reduction in the photo-reaction was estimated using the figure-of-merit scheme developed by the IUPAC [34]. Accordingly, electrical energy per order (E_{EO}) was calculated by considering that E_{EO} equals to the amount of electrical energy (kWh) that should be consumed to remove almost 90% of the pollutant from 1 m^3 of solution [35]. Thus, Eq. (5) was used by considering P (kW), t (min), and V (L) as the rate power of the photo-reactor system, the irradiation time, and solution volume inside the reactor, respectively. In addition, E_{EO} was estimated from the kinetics data by combining Eqs. (4) and (6) in the form of Eq. (7).

$$E_{EO} = \frac{P \times t \times 1,000}{V \times 60 \times \log \frac{C_i}{C_f}} \tag{6}$$

$$E_{EO} = \frac{P \times 38.4}{V \times K_{obs}} \tag{7}$$

3. Results and discussion

3.1. CCD design and fitting a response-surface model

The un-coded values of the independent variables and the predicted and experimental values of the dependent response, that is, reduction efficiency, according to the 28 runs of CCD are listed in Table 2.

The coded experimental data were fitted into the three FO, TWI, and FSO models. The modeling results and the related statistical measures, including lack-of-fit, F-statistic, R-squared, adjusted R-squared, AIC, and p-value, are summarized in Table 3.

The determined terms of the models were used to specify the response-surface portions of the models. Since the employed dataset was comprised of the coded data, the models provided some information about the direction of the steepest ascent as the stationary points. The presence of the stationary points indicated an approximate set of optimal conditions in the RSM evaluations. Lack of fit measures variations in the data around the fitted model. This measurement should be insignificant for a well-fitted model [36]. Comparison of the statistical results of the three applied models showed that the three models involved insignificant lack-of-fit with small p-values (Table 3) while lack-of-fit of the FSO model was higher level. Consequently, it was not required to describe these models based on their information about the un-coded stationary points. To achieve a model with a higher level of lack-of-fit insignificance, the obtained models were reduced. In this way, the X_4 variable of the PQ term and X_2, X_3 variables of the TWI term of the full second-order model were removed. The lack-of-fit value of the resultant full second-order model was insignificant and its p-value was about 0.6711, which indicated a well-fitted model.

3.2. Regression analysis

Table 4 presents the ANOVA results of the CCD. According to Table 4, the highest R^2 value (multiple R^2: 0.9986 and adjusted R^2: 0.9974), the lowest P-value (2.2×10^{-16}), the lowest AIC (12.27) and the most insignificant lack-of-fit (0.6711) correspond to the second-order model. Therefore, the RFS model is the most appropriate model for describing uptake of Cr ions by PCR, and it can be employed for optimization and prediction of the reduction process. The regression results of the quadratic RFS model with the un-coded values of the four X_1–X_4 variables are reported below. The equations that resulted from implementing the actual parameters in the quadratic model are:

Final equation in terms of actual factors:

$$\Upsilon = 66.09571 + 6.99167X_1 + 6.335X_2 + 17.87X_3 - 16.78833X_4 - 4.7X_1X_2 - 2.61X_1X_3 - 8.435X_1X_4 + 1.9X_2X_3 - 22.574X_1^2 - 11.364X_3^2 + 15.52595X_4^2 \tag{8}$$

Table 2
Values of the experimental and predicted removal efficiencies

Run	Iodide dose (mg L^{-1})	pH	Time (min)	Cr concentration (mg L^{-1})	Reduction	Fit predict	lwr	Upr
1	0.30	7.00	50.00	2.50	66.25	66.10	64.46	67.73
2	0.20	5.50	30.00	1.50	51.79	51.17	49.25	53.09
3	0.40	8.50	70.00	3.50	65.42	65.58	63.66	67.50
4	0.30	7.00	50.00	2.50	66.61	66.10	64.46	67.73
5	0.20	8.50	70.00	1.50	78.98	78.81	76.89	80.73
6	0.20	5.50	70.00	1.50	69.69	69.52	67.60	71.44
7	0.30	7.00	50.00	2.50	67.52	66.10	64.46	67.73
8	0.20	5.50	30.00	3.50	38.58	38.38	36.46	40.30
9	0.40	8.50	70.00	1.50	86.53	86.36	84.44	88.28
10	0.30	7.00	50.00	2.50	65.52	66.10	64.46	67.73
11	0.20	8.50	30.00	1.50	58.72	58.56	56.64	60.48
12	0.20	8.50	30.00	3.50	46.19	46.46	44.54	48.38
13	0.40	8.50	30.00	1.50	69.53	68.72	66.80	70.64
14	0.40	5.50	30.00	1.50	66.08	66.04	64.12	67.96
15	0.40	5.50	70.00	3.50	60.50	60.29	58.38	62.21
16	0.40	8.50	30.00	3.50	48.39	48.19	46.27	50.11
17	0.30	7.00	50.00	2.50	65.49	66.10	64.46	67.73
18	0.30	7.00	50.00	2.50	65.99	66.10	64.46	67.73
19	0.20	8.50	70.00	3.50	66.79	66.46	64.54	68.38
20	0.40	5.50	30.00	3.50	45.09	44.81	42.89	46.73
21	0.30	7.00	50.00	2.50	65.29	66.10	64.46	67.73
22	0.40	5.50	70.00	1.50	82.50	81.78	79.86	83.69
23	0.20	5.50	70.00	3.50	56.12	56.48	54.56	58.39
24	0.50	7.00	50.00	2.50	49.79	50.51	48.59	52.43
25	0.30	7.00	50.00	4.50	65.03	64.83	62.91	66.75
26	0.10	7.00	50.00	2.50	36.43	36.53	34.61	38.45
27	0.30	7.00	90.00	2.50	72.39	72.60	70.68	74.52
28	0.30	4.00	50.00	2.50	60.16	60.69	58.77	62.61
2	0.30	10.00	50.00	2.50	73.07	73.36	71.44	75.28
30	0.30	7.00	10.00	2.50	36.25	36.86	34.94	38.78
31	0.30	7.00	50.00	0.50	97.39	98.41	96.49	100.00

Table 3
Comparison of different models of RSM for fitting a response-surface model

	Multiple R-squared	Adjusted R-squared	F-statistic	p-value	AIC	Lack of fit
First-order response-surface model	0.6942	0.6471	14.75 on 4 and 26 DF	2.053e-06	97.11	1.774e-06
Two-way interactions model	0.7116	0.5675	4.936 on 10 and 20 DF	0.001187	128.41	8.115e-07
Second-order model	0.9986	0.9974	21.8 on 14 and 16 DF	2.2e-16	12.27	0.6711

3.3. Process optimization and confirmation

As mentioned above, the RFS model was selected as the best-fitted model. Consequently, the RFS model was adopted to optimize the process. Based on this model, the stationary points for iodide dose (mg L^{-1}), pH, time (min), and initial Cr concentration were 0.3 mg L^{-1}, 7, 50 min, and 0.5 mg L^{-1}, respectively. These stationary points can be considered as approximations of the optimal conditions. By performing simultaneous optimization of the four parameters, the maximum reduction efficiency was obtained as 94.43% at the experimental conditions. The optimal condition determined by RSM was validated by carrying out an additional experiment. As Table 5 shows, the experimental response and the value predicted by the RFS model was close (error: 2.11% and standard deviation: ±2.42%).

Table 4
Analysis of variance (ANOVA) for the second-order model

Model formula in RSM	DF	Sum of squares	Mean square	F-value	Probability (P)
First-order response (x_1, x_2, x_3, x_4)	4	4,141.2.6	1,035.30	1,999.3751	<2.2e-16
Two-way interaction response (x_1, x_2, x_3, x_4)	6	104.2	17.37	33.5491	3.396e-08
Pure quadratic response (x_1, x_2, x_3, x_4)	4	1,712.0	428.00	826.5607	<2.2e-16
Residuals	16	8.3	0.52	–	–
Lack of fit	10	4.6	0.46	0.7524	0.6711
Pure error	6	3.7	0.61	–	–

Multiple R-squared: 0.9986, Adjusted R-squared: 0.9974, F-statistic: 821.8 on 14 and 16 DF, p-value: <2.2e-16

Table 5
Experimental and predicted values (by RSM) at the optimal condition

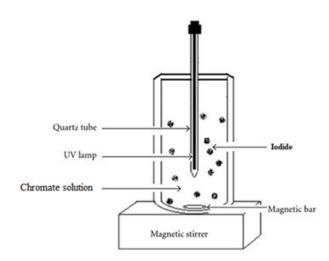| Iodide dose (mg L^{-1})	pH	Time (min)	Cr^{6+} concentration	Cr^{6+} reduction (%)	
				Predicted (%)	Experimental (%)
0.3	7	50	0.5	98.41	94.34

Fig. 1. Schematic view of the photo-reactor setup.

3.4. Response surface plots

Interaction effect of the dependent variables on the photo-precipitation efficiency is expressed by the contour plotting. Solution time is most important parameters reflecting the reduction capacity of Cr by UV methods. As shown in Fig. 2a, the photo-precipitation rate improves with increasing time. However, it reduces the efficiency due to increasing of Cr concentration prevention of light passage. As indicated in Figs. 2b and c, by increasing the concentration of the iodide the photo-precipitation rate was improved. Nevertheless, with the increasing iodide and Cr concentration, the efficiency decreased and the reason could be lack of adequate iodide for the chromium reduction. As seen in Fig. 2c, with the increasing of pH, the photo-precipitation was improved. In addition, by increasing the time, the percentage of photo-precipitation increased, and at interaction of time-pH, this increase was improved. The reaction is facilitated by increasing the process time of transforming the iodide into hydrate electrons, which improved the photo-precipitation of chromium from the solution. So that, altering the pH level of the Cr solution from 3 to 11 increases the photo-precipitation efficiency of this method. The low pH values electron hydrate rapidity recombination with OH radical at the high.

3.5. Effect of Cr concentration, kinetics, and consumed energy

The rate and rate constants of the process were calculated at divers' initial Cr concentration from 5 to 20 mg L^{-1} after 2.5 to 15 min reaction time to investigate the potential of UI procedure in Cr photo-precipitation. As shown in Fig. 3, by calculating the slope of plot $\ln(C_t/C_0)$ vs. t the k_{obs} (reaction rate constant) was obtained. In addition, the observed rate (mg L^{-1} min^{-1}) of Cr photo-precipitation in the photo-reactor is shown by r_{obs}. It should be noted that the reaction rate is constantly positive and a negative value due to declining reactant concentration. For diverse Cr concentrations, the PFO rates of Cr photo-precipitation through UI photoreactor is displayed in Table 6 [37–39]. Values of E_{EO} were predicted according to the kinetic model and experimental data and the listed values were obtained via kinetics data [Eqs. (9) and (10)]. As shown in Table 6, the value of R^2 is above 0.96 that shows the reliable fit into the PFO kinetic model for the experimental rate data of Cr removal via the UI process [37]. Additionally, it specifies that in UI procedure, Cr initial concentration directly affected Cr removal [40]. As shown in Table 6, k_{obs} (min^{-1}) and r_{obs} (mg L^{-1} min^{-1}) varies from 0.1186 to 0.0728 and from 3.64 to 23.72, respectively, which is proportional to the increase in the initial concentration of Cr from 50 to 200 mg L^{-1}. Because of these sensible changes, the probability of effective contact between the Cr molecules and the available reductive and oxidative species in solution increased with the increase in Cr concentration, and therefore the reaction rate was improved [41]. In addition, E_{EO} declined from 11.60 to 7.12 kW h m^{-3} because of the enhanced effective contacts (increasing of reaction rate) and energy levels
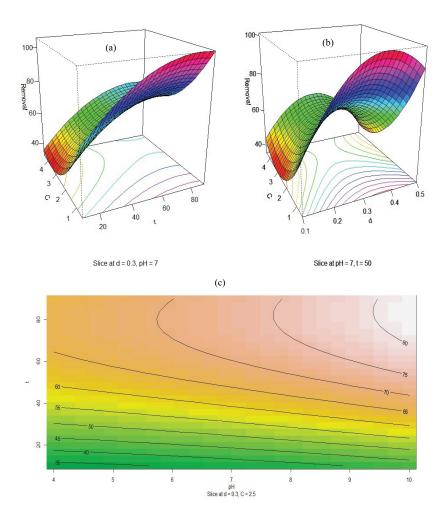
Fig. 2. Response surface plot of the Cr reduction as the function of (a) Cr concentration/time, (b) Cr concentration/iodide dose, and (c) pH/time.
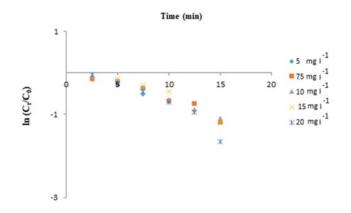

Fig. 3. $\ln(C_t/C_0)$ vs. t to calculate reaction rate constant (at optimal condition).

have been presented, since E_{EO} amounts differed with Cr concentration. At higher concentrations declines the amount of consumed energy for Cr photo-precipitation. There is a similarity of E_{EO} value related to UI procedure and reported values for degradation of 4 mg L^{-1} TCS via the electrochemical process (0.466–2.225 kWh m^{-3}) [42] and carbofuran degradation by photocatalyst was 124.8 to 540.3 kWh m^{-3} [43]. As reported in Table 6, figure-of-merit E_{EO} varies from 3.76–6.69 (for 5 mg L^{-1}) to 3.31–21.35 (for 20 mg L^{-1}) kWhm^3, respectively, by increasing Cr concentration from 5 to 20 mg L^{-1}. Similarly, by changing the concentration of Cr from 5 to 20, the energy consumption was from 11.60 to 7.12 kWh m^{-3} and from 5.22 to 12.33 kWh m^{-3} in kinetic and figure-of-merit models, respectively.

Based on this model, the stationary points for the stationary points for iodide dose (mg L^{-1}), pH, time (min), and initial Cr concentration were 0.3 mg L^{-1}, 7, 50 min, and 0.5 mg L^{-1}, respectively, and photo-precipitation performance reached to 94.42%. The computational results showed that the increased concentration of the Cr solution from 5 to 20 mg L^{-1} decreased the observed rate constant (k_{obs}) from 0.0634 to 0.1186 min^{-1} while it increased the photoreaction rate (r_{obs}) from 0.3317 to 2.372 mg L^{-1} min^{-1}. Finally, varying the Cr concentration from 5 to 20 mg L^{-1}, increased E_{EO} from 5.67 to 15.21 (kinetic model) and from 5.11 to 18.45 (figure-of-merit model) kW h m^{-1}.

Table 6
PFO kinetic model and electrical energy consumption

| Cr (mg L^{-1}) | Photo-precipitation | | | | Figure-of-merit |
	R^2	k_{obs} (min^{-1})	r_{obs} (mg L^{-1} min^{-1})	Kinetic E_{EO} (kwh m^{-3})	E_{EO} (kwh m^{-3})
5	0.9649	0.0634	0.3317	5.67	5.11–7.57
7.5	0.9567	0.0727	0.5452	7.41	6.54–8.07
10	0.9854	0.1051	1.051	9.41	7.51–9.67
15	0.9737	0.1236	1.854	12.42	10.21–14.48
20	0.9422	0.1186	2.372	15.21	10.26–18.45

4. Conclusions

In this work, iodide was stimulated by UV irradiation with 254 nm wavelength to create reducer species (H, I$^-$ radicals, and e$_{aq}^-$), and thus the chromate was precipitation. In this study, the effect of iodide dose (X_1), pH (X_2), the time (X_3), and initial concentration of Cr^{VI} (X_4) was investigated. Based on modeling and optimization by R software, the stationary points for the stationary points for iodide dose (mg L^{-1}), pH, time (min), and initial Cr concentration were 0.3 mg L^{-1}, 7, 50 min, and 0.5 mg L^{-1}, respectively. The computational results showed that the increased concentration of the Cr solution from 5 to 20 mg L^{-1} decreased the observed rate constant (k_{obs}) from 0.0634 to 0.1186 min^{-1} while it increased the photoreaction rate (r_{obs}) from 0.3317 to 2.372 mg L^{-1} min^{-1}. Finally, varying the Cr concentration from 5 to 20 mg L^{-1}, increased E_{EO} from 5.67 to 15.21 (kinetic model) and from 5.11 to 18.45 (figure-of-merit model) kWh m^{-3}. This method is a feasible and simple operation that can apply in industrial-scale especially in a water well in urban to protect from people.

Acknowledgment

References

[1] N. Saranya, A. Ajmani, V. Sivasubramanian, N. Selvaraju, Hexavalent chromium removal from simulated and real effluents using *Artocarpus heterophyllus* peel biosorbent-batch and continuous studies, J. Mol. Liq., 265 (2018) 779–790.

[2] A. Maleki, A.H. Mahvi, M.A. Zazouli, H. Izanloo, A.H. Barati, Aqueous cadmium removal by adsorption on barley hull and barley hull ash, Asian J. Chem., 23 (2011) 1373–1376.

[3] A. Mahvi, F. Gholami, S. Nazmara, Cadmium biosorption from wastewater by *Ulmus* leaves and their ash, Eur. J. Sci. Res., 23 (2008) 197–203.

[4] L. Rafati, A.H. Mahvi, A.R. Asgari, S.S. Hosseini, Removal of chromium (VI) from aqueous solutions using Lewatit fo36 nano ion exchange resin, Int. J. Environ. Sci. Technol., 7 (2010) 147–156.

[5] S. Rangabhashiyam, P. Balasubramanian, Adsorption behaviors of hazardous methylene blue and hexavalent chromium on novel materials derived from *Pterospermum acerifolium* shells, J. Mol. Liq., 254 (2018) 433–445.

[6] J. Huang, Y. Li, Y. Cao, F. Peng, Y. Cao, Q. Shao, H. Liu, Z. Guo, Hexavalent chromium removal over magnetic carbon nanoadsorbents: synergistic effect of fluorine and nitrogen co-doping, J. Mater. Chem. A, 6 (2018) 13062–13074.

[7] Z. Zhao, H. An, J. Lin, M. Feng, V. Murugadoss, T. Ding, H. Liu, Q. Shao, X. Mai, N. Wang, Progress on the photocatalytic reduction removal of chromium contamination, Chem. Rec., 19 (2019) 873–882.

[8] H. Guo, C. Bi, C. Zeng, W. Ma, L. Yan, K. Li, K. Wei, *Camellia oleifera* seed shell carbon as an efficient renewable bio-adsorbent for the adsorption removal of hexavalent chromium and methylene blue from aqueous solution, J. Mol. Liq., 249 (2018) 629–636.

[9] M.H. Ehrampoush, M. Miri, M.H. Salmani, A.H. Mahvi, Cadmium removal from aqueous solution by green synthesis iron oxide nanoparticles with tangerine peel extract, J. Environ. Health Sci. Eng., 13 (2015) 84.

[10] H.J. Mansorian, A.H. Mahvi, H.J. Jafari, Removal of lead and zinc from battery industry wastewater using electrocoagulation process: influence of direct and alternating current by using iron and stainless steel rod electrodes, Sep. Purif. Technol., 135 (2014) 165–175.

[11] R. Ebrahimi, A. Maleki, B. Shahmoradi, H. Daraei, A.H. Mahvi, A.H. Barati, A. Eslami, Elimination of arsenic contamination from water using chemically modified wheat straw, Desal. Water Treat., 51 (2013) 2306–2316.

[12] E. Bazrafshan, A.H. Mahvi, M.A. Zazouli, Removal of zinc and copper from aqueous solutions by electrocoagulation technology using iron electrodes, Asian J. Chem., 23 (2011) 5506–5510.

[13] F. Liu, J. Liang, L. Chen, M. Tong, W. Liu, Photocatalytic removal of diclofenac by Ti doped BiOI microspheres under visible light irradiation: kinetics, mechanism, and pathways, J. Mol. Liq., 275 (2019) 807–814.

[14] B. Kakavandi, R.R. Kalantary, M. Farzadkia, A.H. Mahvi, A. Esrafili, A. Azari, A.R. Yari, A.B. Javid, Enhanced chromium (VI) removal using activated carbon modified by zero valent iron and silver bimetallic nanoparticles, J. Environ. Health Sci. Eng., 12 (2014) 115.

[15] Y. Zhang, H. Sun, H. Sadam, Y. Liu, L. Shao, Supramolecular chemistry assisted construction of ultra-stable solvent-resistant membranes for angstrom-sized molecular separation, Chem. Eng. J., 371 (2019) 535–543.

[16] N. Zhou, K. Gong, Q. Hu, X. Cheng, J. Zhou, M. Dong, N. Wang, T. Ding, B. Qiu, Z. Guo, Optimizing nanocarbon shell in zero-valent iron nanoparticles for improved electron utilization in Cr(VI) reduction, Chemosphere, 242 (2020) 125235.

[17] X. Xu, H. Zhang, C. Ma, H. Gu, H. Lou, S. Lyu, C. Liang, J. Kong, J. Gu, A superfast hexavalent chromium scavenger: magnetic nanocarbon bridged nanomagnetite network with excellent recyclability, J. Hazard. Mater., 353 (2018) 166–172.

[18] A. Asgari, F. Vaezi, S. Nasseri, O. Dördelmann, A. Mahvi, E.D. Fard, Removal of hexavalent chromium from drinking water by granular ferric hydroxide, J. Environ. Health Sci. Eng., 5 (2008) 277–282.

[19] C. Bao, M. Chen, X. Jin, D. Hu, Q. Huang, Efficient and stable photocatalytic reduction of aqueous hexavalent chromium ions by polyaniline surface-hybridized ZnO nanosheets, J. Mol. Liq., 279 (2019) 133–145.

[20] E. Bazrafshan, L. Mohammadi, A. Ansari-Moghaddam, A.H. Mahvi, Heavy metals removal from aqueous environments by electrocoagulation process–a systematic review, J. Environ. Health Sci. Eng., 13 (2015) 74.

[21] M. Chigondo, H.K. Paumo, M. Bhaumik, K. Pillay, A. Maity, Magnetic arginine-functionalized polypyrrole with improved and selective chromium (VI) ions removal from water, J. Mol. Liq., 275 (2019) 778–791.

[22] W. Liu, L. Jin, J. Xu, J. Liu, Y. Li, P. Zhou, C. Wang, R.A. Dahlgren, X. Wang, Insight into pH dependent Cr (VI) removal with magnetic Fe_3S_4, Chem. Eng. J., 359 (2019) 564–571.

[23] M. Sarkhosh, M. Sadani, M. Abtahi, H. Azarpira, H. Alidadi, Z. Atafar, S. Rezaei, S.M. Mohseni, N. Vaezi, Y. Fakhri, Photo-biological degradation of bisphenol A, UV/ZnO/iodide process at the center of biological reactor, J. Photochem. Photobiol., A, 374 (2019) 115–124.

[24] H. Azarpira, M. Sadani, M. Abtahi, N. Vaezi, S. Rezaei, Z. Atafar, S.M. Mohseni, M. Sarkhosh, M. Ghaderpoori, H. Keramati, Photo-catalytic degradation of triclosan with UV/iodide/ZnO process: performance, kinetic, degradation pathway, energy consumption and toxicology, J. Photochem. Photobiol., A, 371 (2019) 423–432.

[25] Z. Sun, C. Zhang, P. Chen, Q. Zhou, M.R. Hoffmann, Impact of humic acid on the photoreductive degradation of perfluorooctane sulfonate (PFOS) by UV/iodide process, Water Res., 127 (2017) 50–58.

[26] Z. Sun, C. Zhang, X. Zhao, J. Chen, Q. Zhou, Efficient photoreductive decomposition of N-nitrosodimethylamine by UV/iodide process, J. Hazard. Mater., 329 (2017) 185–192.

[27] H. Kashudhan, A. Dixit, A. Upadhyay, Optimization of ingredients for the development of wheatgrass based therapeutic juice using response surface methodology (RSM), J. Pharmacogn. Phytochem., 6 (2017) 338–345.

[28] S. Murcia-López, K. Villa, T. Andreu, J.R. Morante, Improved selectivity for partial oxidation of methane to methanol in the presence of nitrite ions and $BiVO_4$ photocatalyst, Chem. Commun., 51 (2015) 7249–7252.

[29] C.-Y. Chu, M.H. Huang, Facet-dependent photocatalytic properties of Cu_2O crystals probed by using electron, hole and radical scavengers, J. Mater. Chem. A, 5 (2017) 15116–15123.

[30] A. Sheikhmohammadi, Z. Dahaghin, S.M. Mohseni, M. Sarkhosh, H. Azarpira, Z. Atafar, M. Abtahi, S. Rezaei, M. Sardar, H. Masoudi, The synthesis and application of the $SiO_2@Fe_3O_4@MBT$ nanocomposite as a new magnetic sorbent for the adsorption of arsenate from aqueous solutions: modeling, optimization, and adsorption studies, J. Mol. Liq., 255 (2018) 313–323.

[31] D. Podstawczyk, A. Witek-Krowiak, A. Dawiec, A. Bhatnagar, Biosorption of copper (II) ions by flax meal: empirical modeling and process optimization by response surface methodology (RSM) and artificial neural network (ANN) simulation, Ecol. Eng., 83 (2015) 364–379.

[32] M.E.M. Ali, H. Abdelsalam, N.S. Ammar, H.S. Ibrahim, Response surface methodology for optimization of the adsorption capability of ball-milled pomegranate peel for different pollutants, J. Mol. Liq., 250 (2018) 433–445.

[33] A. Sheikhmohammadi, S.M. Mohseni, M. Sardar, M. Abtahi, S. Mahdavi, H. Keramati, Z. Dahaghin, S. Rezaei, M. Almasian, M. Sarkhosh, Application of graphene oxide modified with 8-hydroxyquinoline for the adsorption of Cr(VI) from wastewater: optimization, kinetic, thermodynamic and equilibrium studies, J. Mol. Liq., 233 (2017) 75–88.

[34] C.-G. Lee, H. Javed, D. Zhang, J.-H. Kim, P. Westerhoff, Q. Li, P.J. Alvarez, Porous electrospun fibers embedding TiO_2 for adsorption and photocatalytic degradation of water pollutants, Environ. Sci. Technol., 52 (2018) 4285–4293.

[35] N. Daneshvar, A. Aleboyeh, A. Khataee, The evaluation of electrical energy per order (EEo) for photooxidative decolorization of four textile dye solutions by the kinetic model, Chemosphere, 59 (2005) 761–767.

[36] M.A. da Silva, S.G. Gilmour, L.A. Trinca, Factorial and response surface designs robust to missing observations, Comput. Stat. Data Anal., 113 (2017) 261–272.

[37] T.M. Berhane, J. Levy, M.P. Krekeler, N.D. Danielson, Kinetic sorption of contaminants of emerging concern by a palygorskite-montmorillonite filter medium, Chemosphere, 176 (2017) 231–242.

[38] S. Eris, S. Azizian, Analysis of adsorption kinetics at solid/solution interface using a hyperbolic tangent model, J. Mol. Liq., 231 (2017) 523–527.

[39] T.A. Saleh, M. Tuzen, A. Sarı, Polyamide magnetic palygorskite for the simultaneous removal of Hg(II) and methyl mercury; with factorial design analysis, J. Environ. Manage., 211 (2018) 323–333.

[40] X. Liu, J. Zhong, L. Fang, L. Wang, M. Ye, Y. Shao, J. Li, T. Zhang, Trichloroacetic acid reduction by an advanced reduction process based on carboxyl anion radical, Chem. Eng. J., 303 (2016) 56–63.

[41] M. Massoudinejad, S.M. Zarandy, M.M. Amini, S.M. Mohseni, Enhancing photo-precipitation of chromate with carboxyl radicals: kinetic, energy analysis and sludge survey, Process Saf. Environ. Prot., 134 (2020) 440–447.

[42] D. Maharana, J. Niu, N.N. Rao, Z. Xu, J. Shi, Electrochemical degradation of triclosan at a Ti/SnO₂-Sb/Ce-PbO₂ anode, Clean Soil Air Water, 43 (2015) 958–966.

[43] M. Vishnuganth, N. Remya, M. Kumar, N. Selvaraju, Photocatalytic degradation of carbofuran by TiO_2-coated activated carbon: model for kinetic, electrical energy per order and economic analysis, J. Environ. Manage., 181 (2016) 201–207.